Journal of Solid State Chemistry 301 (2021) 122319

Contents lists available at ScienceDirect

Journal of Solid State Chemistry

journal homepage: www.elsevier.com/locate/jssc

Growth, single crystal investigation, hirshfeld surface analysis, DFT studies, molecular docking, physico-chemical characterization and, in vitro, antioxidant activity of a novel hybrid complex

Yathreb Oueslati [a], Youness El Bakri [b], Arto Valkonen [c], Carlos J. Gómez García [d], El Hassane Anouar [e], Wajda Smirani [a,*]

[a] *Laboratory of Chemical Materials, Faculty of Sciences of Bizerte, Carthage University, 7021, Zarzouna, Tunisia*
[b] *South Ural State University, Lenin Prospect 76, Chelyabinsk, 454080, Russian Federation*
[c] *Department of Chemistry, University of Jyvaskyla, 40014, Jyvaskyla, Finland*
[d] *Instituto de Ciencia Molecular (ICMol), University of Valencia, Spain*
[e] *Department of Chemistry, College of Science and Humanities in Al-Kharj, Prince Sattam Bin Abdulaziz University, Al-Kharj, 11942, Saudi Arabia*

ARTICLE INFO

Keywords:
Transition metal
Co(II) diphosphate cluster
Optimized geometry
Magnetic properties
Molecular docking

ABSTRACT

Interaction of the diphosphoric acid ($H_4P_2O_7$) and organic ligand (3.4-dimethylaniline) with transition metal ions, cobalt (II) chloride leads to the formation of novel stable Co(II)-diphosphate cluster with empirical formula $(C_8H_{12}N)_2[Co(H_2P_2O_7)_2(H_2O)_2].2H_2O$. The structure of the synthesized material was confirmed by single crystal XRD at 120 K. The crystal was plate and crystallized in the triclinic P $\overline{1}$ space group with a = 7.5340(4) Å, b = 7.5445(4) Å, c = 13.6896(8) Å, α = 84.215(5)°, β = 76.038(5)°, γ = 74.284(5)°, V = 726.38(7) $Å^3$ and Z = 1. Full-matrix least-squares refinement converged at R = 0.035 and Rw = 0.088 for 3636 independent observed reflections. Indeed, the purity phase was confirmed by the powder X-ray diffraction. A detailed analysis of the intermolecular close interactions and their percentage contribution has been performed based on the Hirshfeld surfaces and their associated two-dimensional fingerprint plots. In this context, spectroscopic studies were performed to distinguish the different chemical functional groups and their environments in this molecule. To determine the optical properties, the UV–Visible and luminescence behavior were investigated. The magnetic properties have been investigated in the temperature range 2–300 k. The geometry of the hybrid complex was optimized in the gas phase, using density functional theory (B3LYP) with the 6-31+G (d,p) basis sets, it is found that the calculated and the experimental results were in good consistency. Furthermore, the synthesized product was screened for its antioxidant activities. Molecular docking study was additionally carried.

1. Introduction

Historically speaking, Mother Earth is considered as an ancient example of the creation of hybrid materials. The latter, are known as a structure that gathers the desirable properties of both the organic and mineral components in a single phase [1]. The birth of hybrid organic-inorganic materials was spontaneously since hundreds of millions years earlier than we knew. Thus, this concept has monopolized the attention of scientists and inspired them to start manmade these compounds with extraordinary new physicochemical properties.

Thanks to their well diversified structural, richer geometry and new behavior, those materials have drawn great interest and are often employed in wide applications like pharmaceutical industries [2,3], optics [4–8], and catalysis [9].

Quite recently, a keen interest is focused on the integration of various transition metal ions with hybrid compounds, as a result of not only their excellent biological activities due to chelation [10] but also for their chemical and physical properties. To taking advantage of all these technologically distinctive properties, researchers have been vigorously used these complexes in many scientific areas and importantly within medicinal biochemistry, where a lot of metal-based drugs have been used with diverse therapeutic activity [11–16]. Notably, platinum was among the first metals used as essential drugs in 50–70% of all cancer chemotherapy [17–19]. Up till now, three platinum complexes are used

---

* Corresponding author.
E-mail address: wajda_sta@yahoo.fr (W. Smirani).

https://doi.org/10.1016/j.jssc.2021.122319
Received 31 March 2021; Received in revised form 24 May 2021; Accepted 30 May 2021

clinically, starting with cisplatin *cis*-[$Pt(NH_3)_2Cl_2$] which has been available since 1978 [20], and the two other platinum (II) complexes were carboplatin and oxaliplatin. Besides platinum, other transition metals such as titanium was employed with the same aim and acted as an anticancer drug against breast and gastrointestinal carcinomas [21]. Also, many scientists and pharmacological works have found that gold is a good therapeutic potential of rheumatoid arthritis (RA) [22] such as joint pain and swelling. Additionally, Transition metal complexes of vanadium have been extensively explored for diabetes treatment by decreasing the level of hyperglycemia [23].

In this way, some Co(II) complexes have been combined with a variety of base ligands and have been evolved enormously in a great number of areas such as catalysis [24], antibacterial activity [25], separation and encapsulation. From a physical point of view, Co(II) complexes are excellent candidates in the field of magnetism [26], because they have showed a high ability to serve as strong models of magnetic behavior. This behavior is related, in particular, to the single-ion Co(II) with the electronic configuration 3d7, the strong first-order spin-orbit coupling and the ground spin state ($S = 3/2$) [27,28]. In this aspect, several cobalt(II)-based complexes have been reported in numerous coordination geometries. This work is particularly focused on composite where the Co(II) arising in octahedral coordinate.

Furthermore, organic amines play a pivotal role in the design and the determination of the final structures. Among the different types of amines, aniline with the formula $C_6H_5NH_2$ and its derivates are intensively used as structure-directing agents in the synthesis. The latter are weak bases and consist of a benzene ring attached to an amino group. In this context, aniline and substituted anilines can be applied in numerous fields such as pharmaceuticals, pesticides, dyes and pigments [29].

Oxidative stress (OS) is occurred by an imbalance between oxidant and antioxidant species at the cellular or individual level [30]. This imbalance is generated directly from the high level of reactive oxygen species (ROS) in cells, which can cause serious chronic diseases that is cancer, aging, diabetes and coronary heart disease [31,32]. Therefore, the search for new antioxidant agents, prevent or reduce the impact of oxidative stress, has been the subject of intense research. In particular, transition metal complexes are of special interest due to their highly efficient antioxidant activities. Among these synthetic complexes, the cobalt (II) complexes have showed very interesting antioxidant results [33,34].

Herein, we report the preparation of $(C_8H_{12}N)_2[Co(H_2P_2O_7)_2(H_2O)_2].2H_2O$ through the method of crystallization. Foremostly, an analysis by single-crystal X-ray diffraction has been undertaken in order to reach a fine description of the architecture of the title compound and provide valuable informations about the internal lattice (unit cell dimensions, bond-lengths, bond-angles) then the structure was optimized at DFT/B3LYP method with the 6-31+G (d,p) basis sets in order to better understand the molecular bonds and its relationship in observing the spectral features. The information about intermolecular interaction was examined by using Hirshfeld surface analysis. Frontier orbitals and molecular electrostatic potential of the title compound have been calculated. Moreover, the optical and magnetic properties have been also well discussed in detail. The antioxidant activities were determined. Finally, Molecular docking studies were performed between the newly synthesized compound and peroxiredoxin 5 enzymes.

2. Experimental

2.1. Crystal chemistry

Plate and colorless single crystals of the title compound were synthesized at room temperature by the reaction of diphosphoric acid $H_4P_2O_7$ (2.8 mmol, ≥95%), $CoCl_2$ (1.4 mmol, 97%) and 3.4-dimethylaniline (5.61 mmol, 98%) carried out in an acidic medium. The diphosphoric acid was produced from $Na_4P_2O_7$ by using an ion-exchange resin (Amberlite IR 120) in its H-state.

Table 1
Crystal data and experimental parameters used for the intensity data collection strategy and final results of the structure determination.

Empirical formula	$(C_8H_{12}N)_2[Co(H_2P_2O_7)_2(H_2O)_2].2H_2O$
Formula weight	727.28 (g mol^{-1})
Temperature (K)	120
Wavelength (A °)	0.71073
Crystal system	Triclinic
Space group a (Å)	$P\bar{1}$
b (Å)	7.5340(4)
c (Å)	7.5445(4)
α(°)	13.6896(8)
β(°)	84.215(5)
γ(°)	76.038(5)
Volume ($Å^3$)	74.248(5)
Z	726.38(7)
D_{calc} (g cm^{-3})	1
Absorption coefficient	1.663
F (000)	0.892 (mm^{-1})
Theta range for data collection	377
Crystal size (mm^3)	2.807° - 29.865°
Limiting indices	0.10 × 0.08 × 0.04
Reflections collected	$-9<h < 9$, $-9<k < 10$, $-13<l < 19$
Reflections observed	6162
Goodness-of-fit on F^2	3097
Final R indices	1.09
Largest diff. peak and hole (e $Å^{-3}$)	$R_1 = 0.035$ and $wR_2 = 0.1527$
	0.50 and -0.35

Table 2
Hydrogen-bond geometry (Å, °) of $(C_8H_{12}N)_2[Co(H_2P_2O_7)_2(H_2O)_2].2H_2O$ with estimated standard deviation in parentheses.

D-H … . … … A	D-H(Å)	H … A(Å)	D … A(Å)	D-H … A(°)
O(2)–H(20) … $O(5)^{ii}$	0.824(17)	1.752(17)	2.574(2)	175(3)
O(6)–H(60) … $O(3)^{iii}$	0.841(16)	1.719(17)	2.557(2)	174(3)
O(8)–H(80) … $O(5)^{ii}$	0.848(17)	1.920(18)	2.764(2)	173(3)
O(8)-H(8P)···$O(3)^{iv}$	0.817(17)	2.095(18)	2.904(2)	170(3)
O(9)-H(9A) … $O(5)^{iii}$	0.842(17)	2.094(18)	2.924(2)	169(3)
O(9)-H(9B)···$O(3)^{v}$	0.825(16)	2.033(18)	2.849(2)	170(3)
N(1)-H(1A) … O(1)	0.908(16)	1.992(19)	2.802(2)	148(2)
N(1)-H(1B) ···$O(2)^{v}$	0.881(16)	2.46(2)	3.091(2)	129(2)
N(1)-H(1B) ···$O(7)^{i}$	0.881(16)	2.17(2)	2.887(2)	139(2)
N(1)-H(1C) ···O(9)	0.901(16)	1.911(17)	2.799(2)	168(3)

Symmetry codes: (i) -x+1, -y+1, -z+1; (ii) -x+2, -y+1, -z+1; (iii) -x+1, -y+2, -z+1; (iv) x, y-1, z; (v) x-1, y, z.

The resulting solution was stored at room temperature, after several days of slow evaporation the as grown crystals appeared.

2.2. Crystal structure

Single crystal X-ray diffraction measurement was carried out on a SuperNova diffractometer equipped with a MoKα anticathode and a graphite monochromator ($\lambda = 0.71073$ Å) radiation. Crystal structures were solved with direct method SHELXT [35] and refined by full-matrix least squares technique on F^2 using SHELXL2018/1 software [36]. 6162 are the total number of measured reflections of which 3636 reflections are independent. The non-hydrogen atoms were refined anisotropically. All hydrogen atoms were situated in geometrically optimized positions and treated as riding atoms. The molecular plots were created using the DIAMOND program [37]. The details of data collection for the new material are summarized in Table 1. The geometrical characteristics of the hydrogen bonds are listed in Table 2.

X-ray powder diffraction (XRD) measurements were collected using a BRUKER D8-advance diffractometer with CuKα radiation ($\lambda = 1.5406$ Å) at a scanning speed of 2°/min over the 2θ angular range from 0 to 40°.

In order to visualize and explore the intermolecular interactions in the crystal of the title compound, a Hirshfeld surfaces mapped with d_{norm} and their associated two-dimensional fingerprint were constructed from

CIF file and were plotted using Crystal Explorer (version 3.1) software [38].

2.3. Computational methodology

Density functional theory (DFT) is one of the standard computational tools and one of the most important steps to predict the correct geometric structure to get reliable results. Indeed, ground state (GS) geometry optimization and frequency calculations of the title compound were accomplished by means of the Gaussian 16 software [39], the optimized geometry is true minimum. The maximum electronic absorption bands were calculated using TD-DFT at the same level of theory, i.e., B3LYP/6-31+G(d,p). ESP surface is obtained at the same level of theory. The solvent effects are taken into consideration using the polarizable continuum model (IEFPCM) [40].The structure based on the crystallographic data in the supplementary table was used as starting points at the density functional theory (DFT) with the Becke-three-parameter hybrid exchange functional combined with the Lee-Yang-Parr correlation functional (B3LYP) levels under the 6-31+G(d,p) basis set.

2.4. Physico–chemical characterization techniques

The infrared absorption spectrum was recorded on pellets containing the milled sample dispersed in a potassium bromide (KBr) (with 95% KBr and 5% powder approximately) at room temperature, using a Nicolet IR200 in the spectral range 4000-400 cm^{-1}. The scanning number was 32.

Solid state UV–Vis absorption spectra were recorded, at room temperature with a PerkinElmer Lambda 35 spectrophotometer over the 200–800 nm range.

The photoluminescence (PL) measurement was carried out, at room temperature, using the PerkinElmer LS55 fluorescence spectrometer equipped with a 450 W xenon lamp as the excitation source using solid sample at room temperature.

Magnetic measurements of the powdered sample were recorded with a MPMS-XL-5 SQUID apparatus (Quantum design) with an applied magnetic field (H) of 0.5 T.

2.5. Determination of antioxidant activities

2.5.1. ABTS (2,2′-azino-bis(3-ethylbenzthiazoline-6-sulfonic acid)) free radical scavenging assay

The ABTS radical cation method, which applies decolorization assays, has been commonly used to evaluate the antioxidant capacities of the product. According to the protocol of Re et al. [41], the $ABTS^{\bullet+}$ was pre-generated a day before by reacting 7 mM ABTS stock aqueous solution with 2.45 mM potassium persulfate ($K_2S_2O_8$) then was incubated overnight for 12 h–16 h in darkness at room temperature so that the color of the solution change from colorless to deep bluish-green. Prior to assay, the formed solution was diluted in methanol to give an absorbance of 0.700 ± 0.025 centered at 734 nm. The decline in absorbance against a methanol blank was recorded. Thereafter, to determine the scavenging activity, 300 μL of methanolic solution of the synthesized compound with different concentrations (0.25, 0.5, 1 mg/mL) was mixed with 3 mL of the $ABTS^{\bullet+}$ solution, absorbances are measured at 734 nm after stored for about 15 min in the dark and at temperature ambient. Ascorbic acid was used as standard. The percentage of ABTS scavenging effect was measured using the following formula:

$$\text{ABTSo}+\ \ \text{scavenging activity}\ \ (\%) = \left[\frac{(A)_{control} - (A)_{sample}}{(A)_{control}}\right] \times 100$$

Where *(A)*$_{control}$ is the absorbance of the control or the blank solution and *(A)*$_{sample}$ is the absorbance measured in the presence of the tested compound. Measurements were run in triplicate, and the presented results are the arithmetic means of the all data were expressed as mean ± standard deviation (SD) of triplicate determinations (n = 3).

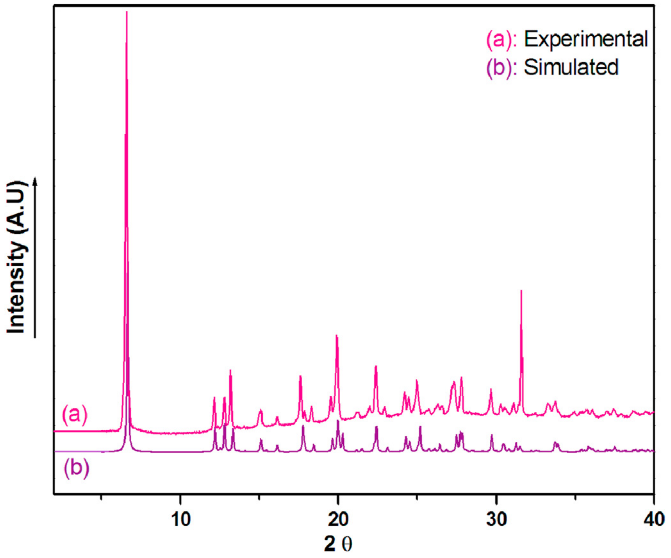

Fig. 1. Experimental and simulated powder XRD patterns of the prepared compound.

2.5.2. Ferrous Ion Chelating (FIC) ability

The ability of sample to chelate ferrous ions was investigated by using FIC method reported by Singh and Rajini [42]. Briefly, a methanolic solution of the studied compound at different concentrations (0.25, 0.5, 1 mg/mL) was mixed with 1 mL of $FeSO_4$ (0.1 mM) followed by 1 mL of ferrozine (0.25 mM). The mixture was shaken vigorously and then left at room temperature for about 10 min. Absorbance was measured spectrophotometrically at 562 nm. The ascorbic acid (AA) used in this bioassay served as a blank control. The ability of extracts to chelate ferrous ions (Fe^{2+}) was calculated by using the equation given below:

$$\text{Chelating effect}\ \ (\%) = \left[\frac{(A)_{control} - (A)_{sample}}{(A)_{control}}\right] \times 100$$

Where *(A)*$_{control}$ and *(A)*$_{sample}$ are the absorbances.

2.6. Docking study

To understand the observed antioxidant activity of name of the compound, molecular docking of the synthesized complex into the active site of the human peroxiredoxin 5 enzyme is investigated using Autodock package [43]. The staring geometries of peroxiredoxin 5 and the original docked ligand benzoic acid were download from the RCSB data bank web site (PDB code 1HD2) [44]. The re-docking of the original ligand into the active site of peroxiredoxin 5 is well reproduced with a RMSD value less than 0.72 Å. Stepwise of molecular docking study is reported in our previous study [45].

3. Results and discussion

3.1. X-ray diffraction study

The X-ray powder diffraction was used to check the structural purity and preferential alignment of the synthesis product, as presented in Fig. 1, the calculated pattern matches well with the observed XRD pattern extrapolated from the single crystal data, confirming the good phase purity of the sample. There is a smooth difference in the positions, widths, and intensities of some peaks can be observed, which are correlated to the different temperatures used for the single crystal (120 K) and powder diffraction measurements (room temperature). Also there

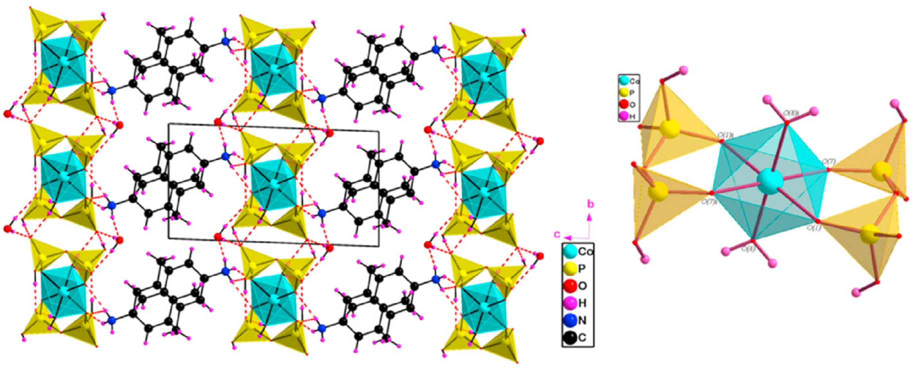

(a) (b)

Fig. 2. (a): A perspective view of $(C_8H_{12}N)_2[Co(H_2P_2O_7)_2(H_2O)_2].2H_2O$ along the C axis exhibiting the alternation of organic and inorganic layers. The dashed red lines bespeak hydrogen bonds. **(b).** A monomeric $[Co(H_2P_2O_7)_2(H_2O)_2]^{2-}$ cluster. (For interpretation of the references to color in this figure legend, the reader is referred to the Web version of this article.)

Table 3
Main bond distances (Å) and bond angles (°) for the CoO_6 octahedron.

Distances Co–O(Å)	Co(1)-O(8)^{i} = 2.0772(15)	
	Co(1)–O(8) = 2.0772(15)	
	Co(1)-O(7)^{i} = 2.0996(14)	
	Co(1)–O(7) = 2.0996(14)	
	Co(1)-O(1)^{i} = 2.1385(14)	
	Co(1)–O(1) = 2.1385(14)	
Angles O–Co–O(°)	O(8)^{i}-Co(1)-O(8) = 180.00(7)	O(7)^{i}-Co(1)-O(1) = 87.66(6)
	O(8)^{i}-Co(1)-O(7)^{i} = 86.88(6)	O(7) -Co(1)-O(1)^{i} = 92.34(6)
	O(8) -Co(1)-O(7)^{i} = 93.12(6)	O(8)^{i}-Co(1)-O(1) = 86.41(6)
	O(8)^{i}-Co(1)-O(7) = 93.12(6)	O(8) -Co(1)-O(8) = 93.59(6)
	O(8) -Co(1)-O(7) = 86.88(6)	O(7)^{i}-Co(1)-O(1) = 92.34(6)
	O(7)^{i}-Co(1)-O(7) = 180.0	O(7) -Co(1)-O(1) = 87.66(6)
	O(8)^{i}-Co(1)-O(1)^{i} = 93.59(6)	O(1)^{i}-Co(1)-O(1) = 180
	O(8) -Co(1)-O(1)^{i} = 86.41(6)	

Symmetry codes: (i) -x+1, -y+1, -z+1.

is some of the extra unexpected lines in the vicinity of 18°, 22°, 35° and 37° with weak intensities are observed which is certainly due to the presence of some impurities in the powder sample, that are absent in the single crystals state.

It can readily be seen in Fig.S1 that the asymmetric unit of the title complex consists of one half of a $[Co(H_2P_2O_7)_2(H_2O)_2]^{2-}$ complex anion, since the Co atom is located on a C_2 axis the other half of the complex is deduced by symmetry, one 3,4-dimethyanilinium cation and one molecule of water.

In the structural arrangement, the metal complex anions are directly connected to the $H_2P_2O_7^{2-}$ groups and the water molecules through hydrogen bonds, leading to a layer of formula $[Co(H_2P_2O_7)_2(H_2O)_2]^{2-}$ perpendicular to the axis $\vec{c}$. The organic part formed by 3,4-dimethyanilinium are sandwiched between these layers as shown in Fig. 2(a).

In the crystal, each cobalt ions Co^{2+} is located on an inversion center and is surrounded by two dihydrogendiphosphate anions fill the equatorial position (Fig. 2(b)) with a bent geometry (P1–O4–P2 = 129.54 (9)°) as observed in other Co(II)-organic diphosphate frameworks [46] and two symmetry-related water molecules filling the axial position, with a Co–O$_{(water)}$ distance of 2.077 (7) Å.

This coordination exhibit a slightly distorted octahedral geometry, where the O1, O7, O1^{i} and O7^{i} ((i): x+1, -y+1, -z+1) atoms constitute the equatorial plane of the octahedron, with a means Co–O bond distance of 2.1053 Å and O–Co–O angles range from 86.41(6) to 180°, these values are adequately close to those observed in other complexes [47]. The main features of the CoO_6 octahedron are presented in Table 3. Going deeper insight in the title compound, each $[Co(H_2P_2O_7)_2(H_2O)_2]^{2-}$ complex anion is interconnected to its adjacent and the free water molecules, via O–H···O hydrogen bonds whose distances are between 2.557(2) and 2.924(2) Å and can be described by four types of graphset motifs $R_4^4(16)$, $R_2^2(12)$, $R_8^4(24)$ and $R_2^1(8)$ (Fig. 3).

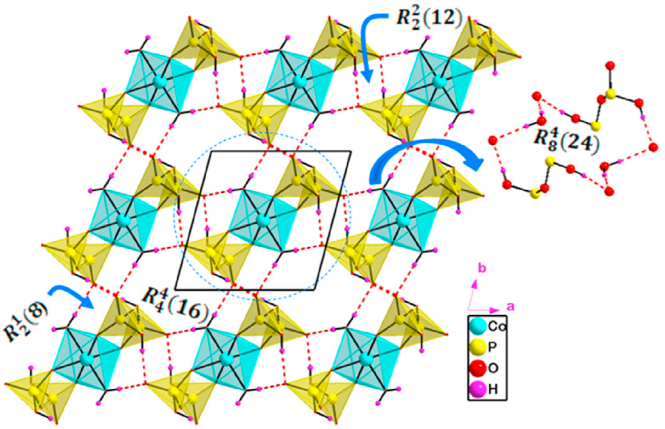

Fig. 3. Crystal packing in the structure and hydrogen bonds ring of the studied compound.

Table 4
Main interatomic distances (Å) and bond angles (°).

$P(1)O_4$ tetrahedron				
P1	O1	O2	O3	O4
O1	***1.5006(15)***	2.543(2)	2.563(4)	2.537(8)
O2	112.65(8)	***1.5545(15)***	2.478(8)	2.519(7)
O3	117.01(8)	108.14(8)	***1.5055(15)***	2.453(7)
O4	109.08(8)	105.30(9)	103.67(8)	***1.6134(16)***
$P(2)O_4$ tetrahedron				
P2	O4	O5	O6	o7
O4	***1.6076(16)***	2.543(10)	2.486(1)	2.531(5)
O5	109.44(8)	***1.5062(15)***	2.473(7)	2.537(4)
O6	102.39(8)	107.51(9)	***1.5594(15)***	2.551(6)
O7	108.92(8)	114.96(8)	112.86(8)	***1.5022(14)***

P(1)–P(2) = 2.914(6)Å P(2)-O(4)-P(1) = 129.54(9)°.

Customarily, inside the PO_4 tetrahedron there are three main types of P–O bond distances. The longest P–O distances correspond to the P–O–P bridge range between 1.6076(16) and 1.6134(16) Å, the intermediate ones relative to the P–O(H) bond are in the range 1.5545(15) - 1.5594 (15) and the shortest ones P–O(E), corresponding to the external oxygen atoms, which spread from 1.5006(15) to 1.562(14). The P–P distance is 2.914(6) Å and the P–O–P is 129.54(9)°(Table 4).

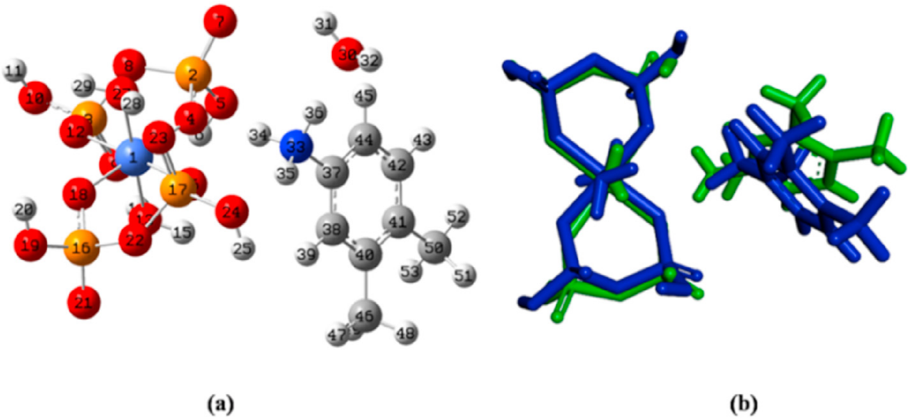

Fig. 4. (a). Optimized geometry of the molecule. **(b).** Superposition between the X-Ray (Green) and optimized structures (Blue) of $(C_8H_{12}N)_2[Co(H_2P_2O_7)_2(H_2O)_2].2H_2O$. (For interpretation of the references to color in this figure legend, the reader is referred to the Web version of this article.)

Table 5
Experimental and calculated selected geometric parameters (Å, °) for the studied compound at the PCM-B3LYP/6–11+G(d,p) level of theory.

	Calculated	Experiment	Variation
Bond lengths (Å)			
Co–O4	1.94295	2.13820	0.20
Co–O12	1.91125	2.09948	0.19
Co–O13	1.93407	2.07723	0.14
Co–O18	1.90145	2.13887	0.24
Co–O26	1.91602	2.09876	0.18
Co–O27	1.92980	2.07745	0.15
P2–O4	1.56381	1.50111	0.06
P2–O5	1.61686	1.55353	0.06
P2–O7	1.48596	1.50555	0.02
P2–O8	1.65327	1.61360	0.04
P3–O8	1.64219	1.60784	0.03
P3–O9	1.51105	1.50556	0.01
P3–O10	1.59386	1.55956	0.03
P3–O12	1.59386	1.50258	0.09
P16–O18	1.55386	1.50032	0.05
P16–O19	1.61319	1.55485	0.06
P16–O21	1.48696	1.50604	0.02
P16–O22	1.66786	1.61265	0.06
P17–O22	1.63003	1.60784	0.02
P17–O23	1.50509	1.50585	0.00
P17–O24	1.60099	1.55956	0.04
P17–O26	1.56193	1.50248	0.06
C37–N33	1.47114	1.47202	0.00
Bond angles (°)			
O26–Co–O4	87.13018	92.34345	5.21
O26–Co–O12	177.85010	179.98118	2.13
O26–Co–O18	91.67996	87.67451	4.01
O26–Co–O13	88.95999	93.11752	4.16
O26–Co–O27	92.55125	86.90971	5.64
O26–P17–O22	114.87041	108.90948	5.96
O26–P17–O23	114.87041	114.94031	0.07
O26–P17–O24	108.56745	112.85948	4.29
O18–P16–O19	105.68788	112.63453	6.95
O18–P16–O21	122.03757	117.00041	5.04
O18–P16–O22	105.18319	109.10380	3.92
O4–P2–O5	107.24367	112.67675	5.43
O4–P2–O7	118.17949	117.01684	1.16
O4–P2–O8	105.76820	109.05172	3.28
Torsion angles (°)			
P17–O26–Co–O4	141.56833	159.53091	17.963
P17–O26–Co–O18	44.04600	20.47790	23.568
P2–O4–Co–O12	8.97137	1.74783	7.224
P2–O4–Co–O13	99.76360	84.96390	14.800
P2–O4–Co–O26	171.23972	178.23700	6.997
P2–O4–Co–O27	78.70123	95.01005	16.309

With regard to the organic motif, the 3,4-dimethyanilinium cations are linked to each inorganic layer, built of $[Co(H_2P_2O_7)_2(H_2O)_2]^{2-}$ anions and the water molecules considered as proton acceptors, through N–H⋯O hydrogen bonds involving the hydrogen atoms of the NH_3^+ groups to maintain the stability of the crystal packing. On this molecule, an anti-periplanar conformations were exhibited by the methyl groups with torsion angle of −179.6(2)° for C8–C4–C5–C6 and -178.9(2)° for C1–C2–C3–C7. The C–C–C and N–C–C angles are around to 120.1 and 119.4°, respectively. In this structure the interaction between two neighboring anti-parallel organic cations with centroid-centroid distances of 7.534 Å which is more than 3.8 Å, the maximum contact for which aromatic–aromatic or π–π interactions are accepted.

The optimized geometry of $(C_8H_{12}N)_2[Co(H_2P_2O_7)_2(H_2O)_2].2H_2O$ have been obtained by using the PCM-B3LYP/6-31+G(d,p) level of theory (Fig. 4(a)). Some of the obtained theoretical geometrical parameters (bond lengths, bond angles and dihedral torsion angles) and the experimental ones are listed in Table 5. Relatively, a good superposition was seen between the computed and experimental data (Fig. 4(b)) that show correlation coefficients of 95–96%. The discrepancies can be explained by the fact that the calculation relates to the isolated molecule where the intermolecular interaction with the neighboring molecules are absent, whereas the experimental result corresponds to interacting molecules in the crystal lattice.

3.2. *Hirshfeld surface analysis*

Hirshfeld surface (HS) is a useful tool to gain insight into understanding the different kinds of intermolecular interactions and to estimate their importance in the crystal packing. The program Crystal Explorer 3.1 was used to visualize and quantify these interactions by calculated the Hirshfeld surfaces [48] and their associated two-dimensional fingerprint plots [49]. The three-dimensional d_{norm} (range of −0.803 to 1.436 Å), which is defined in turns of distance inside d_i, distance outside d_e and the van der Waals radii of the atom, was given by the following equation:

$$d_{norm} = (d_i - r_i^{vdw}) / r_i^{vdw} + (d_e - r_e^{vdw}) / r_e^{vdw}$$

Where r_i^{vdw} and r_e^{vdw} are van der Waals radii of atoms. The normalized contact distance d_{norm}, is portrayed in Fig. 5a, using a color scheme varies from red (distances shorter than the sum of van der Waals radii) through white (distances around the sum of van der Waals radii) to blue (distances longer than the sum of van der Waals radii). The red spots highlight the intermolecular interactions (intercontacts) in the crystalline environment that involve the formation of strong hydrogen bonds between different units of the crystal. The stability of the title compound unit is mainly due to the formation of intramolecular hydrogen bonding that are formed between the hydrogen atom of the ammonium and the oxygen atoms of M − O and water components (Fig. 5(b)).

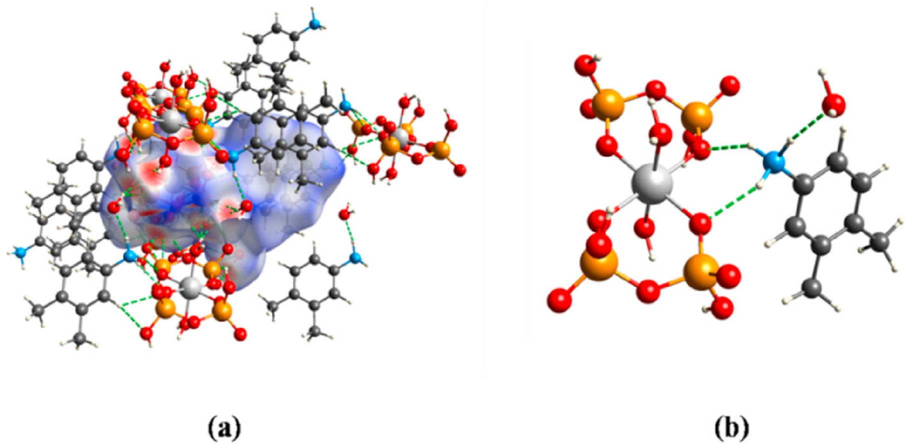

Fig. 5. d_{norm} mapped on the Hirshfeld surface for visualizing the intermolecular hydrogen bonding interactions.

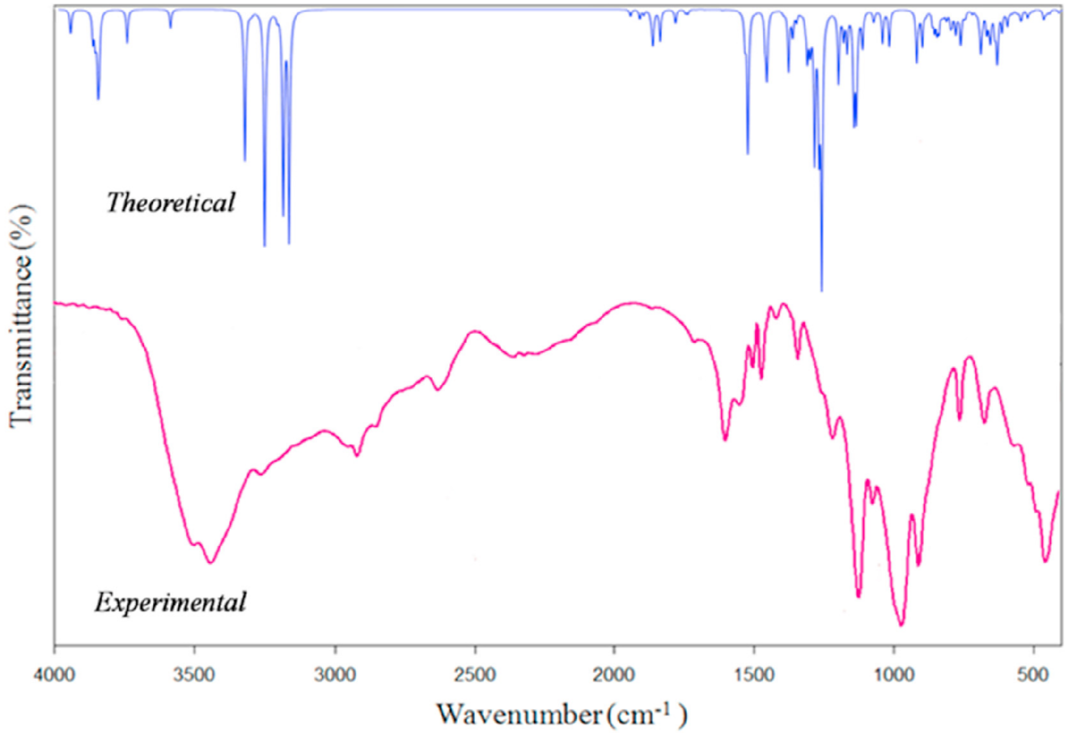

Fig. 6. The DFT computed (blue) and the experimental (pink) IR spectra of the title compound. (For interpretation of the references to color in this figure legend, the reader is referred to the Web version of this article.)

The d_e (range of 0.607–2.679 Å), d_i (range of 0.608–2.672 Å), shape index (range of −1.000 to 1.000 Å), and curvedness (range of −4.000 to 0.400 Å) of the title compound are illustrated in Fig.S2. Two-dimensional fingerprint plots of all the intermolecular contacts of the studied sample are represented in Fig.S3. Indeed, the O⋯H/H⋯O hydrogen bond contacts are the major contributor in the total surface of crystal packing, attains 60%, as can be seen the O⋯H/H⋯O interactions were represented by two symmetrical points at the top left and at the bottom right. The value ($d_e + d_i \sim 1.6$ Å) is less than the sum of van der Waals radii of hydrogen (1.20 Å) and oxygen (1.52 Å) atoms. The H⋯H contacts account for about 29.5% of the total Hirshfeld surface area, it considered as the second most frequent interactions which are appeared with a single broad peak at $d_e = d_i = 1.2$ Å. The value ($d_e + d_i$) is superior to the sum of van der Waals radii of hydrogen atom. Moreover, the C⋯H/H⋯C covers 7.9% of the total Hirshfeld surface, this interactions are occurred as two small sharp spikes in the donor and acceptor area with ($d_e + d_i \sim 2.9$ Å).

Finally the other inter-contacts, C⋯C (1.2%), O⋯O (1.1%) and P⋯O/O⋯P (0.1%) have a smaller contribution of the Hirshfeld surface area.

3.3. *Infrared vibrational study*

FT-IR spectroscopy is one of the sensitive techniques that can smoothly understand the interaction presented in the crystal structure and identify the functional groups. In this study, the theoretical IR spectrum has been calculated using the density functional theory (DFT/B3LYP) method with the 6-31+G(d, p) basis set on the optimized geometries of the compound. Fig. 6 shows both experimentally and theoretically spectra. The experimental wavenumbers confronted to the calculated from the quantum-chemical computations as well as the proposed assignments are summarized in Table 6.

Table 6
Comparaison of some of the observed and calculated vibrational mode frequencies of $(C_8H_{12}N)_2[Co(H_2P_2O_7)_2(H_2O)_2].2H_2O$.

Assignements	*Experimental IR cm-1*	Calculated B3LYP/6-31+G(d,p)	deviations
ν_{as}(OH)	3512	3765	−253
ν_s(OH)	3256	3668	−412
β (OH)	1630	1620	10
ν(N–H)	3264	3390	−126
ν_{ar}(C–H)	3150	3111	39
ν_{as}(C–H–CH3)	2927	2991	−64
ν_s(C–H–CH3)	2855	2940	−85
ν_s(C–H–CH3)	–	2939	−84
ν_{ar}(C=C)	1630	1605	25
ν_{as} (PO3)	1262	1224	38
ν_{as}(POP)	958	945	13
ν_{as}(POP)	805	852	−47
ν_{as}(POP)	–	838	−33
ν_a(POP)	725	705	20
ν_a(POP)	621	680	−59

ν: stretching; β: in-plane bending; as: asymmetric; s: symmetric; ar: aromatic.

3.3.1. The vibration of $H_2P_2O_7^{2-}$

According to other diphosphate results [50–52], the peaks observed between 1262 and 958 cm^{-1}, coming from the symmetric and asymmetric stretching vibrations of the PO_3 terminal show satisfactory agreement with the B3LYP/6-31+G(d,p) scaled values between 1224 and 945 cm^{-1}. It is trustworthy to note that the bands located in the range of 958-805 cm^{-1} are assigned to the asymmetric stretching vibrations ν_{as}(POP) and P–OH modes and the DFT calculations give these modes in the range 945-838 cm^{-1}, while those that appear between 725 and 621 cm^{-1} are attributed to the symmetric stretching vibrations ν_s(POP). These modes are calculated between 705 and 680 cm^{-1} for B3LYP/6-31+G(d,p).

3.3.2. The vibration of water molecule

Essentially, the vibration of the water molecules occurs in three normal modes [53], including symmetric stretching (υ1), asymmetric stretching (υ3) and the in-plane bending (υ2). The broad band spread over a range of 3512-3438 cm^{-1} corresponds to the asymmetric stretching vibrations. The DFT computations give the frequency of these bands at 3765 cm^{-1}. The observed high-wavenumber band around 3256 cm^{-1} is attributed to the symmetric stretching vibrations. The peaks near 1630-1590 cm^{-1} are assignable for the in-plane bending mode. These vibration modes are well reproduced with the B3LYP with a variation of 10 cm^{-1}.

3.3.3. The vibration of $C_8H_{12}N^+$

In the FT-IR experiment spectra, bands between 3512 and 3438 cm^{-1} are assigned to the asymmetric and symmetric stretching modes of the NH_3^+ group [54]. The frequency observed at 3264 cm^{-1} represents the stretching mode of the N–H group. The DFT calculation predicted this mode at 3390 cm^{-1}. The characteristic region for the identification of the C–H stretching vibrations of the aromatic groups is expected to be located in the high frequency range around 3150-3000 cm^{-1} [55] and it is predicted at 3111 cm^{-1} in our DFT calculation. The very weak band located at 2927 cm^{-1} is related to the asymmetric C–H stretching vibration in the methyl group while the band detected at 2855 cm^{-1} is assigned to the symmetric C–H stretching vibration in CH_3. Usually the C–C stretching vibration of aromatic ring occurs at 1630 cm^{-1} [56]. The C=C aromatic stretching modes are identified as seen in Fig. 6 between 1590 and 1510 cm^{-1}. The bands detected at 1382 and 1262 cm^{-1} can be related to the ν(C–N) mode. The bands observed within the range 1164-1118 cm^{-1} pertained to C=C deformation mode. In the present case, the δ (C–N) bending mode is observed at 1012 cm^{-1}. The $C_{(trigonal)}$-H out of plane bending vibrations were appeared in the spectral range 805-725 cm^{-1}.

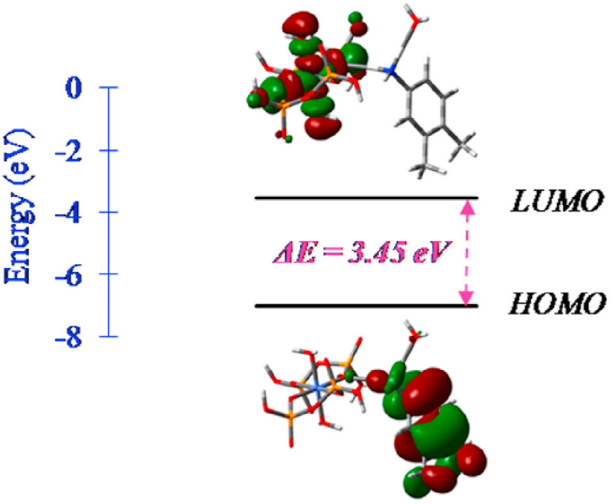

Fig. 7. Molecular orbital surfaces for the HOMO and LUMO of the title compound.

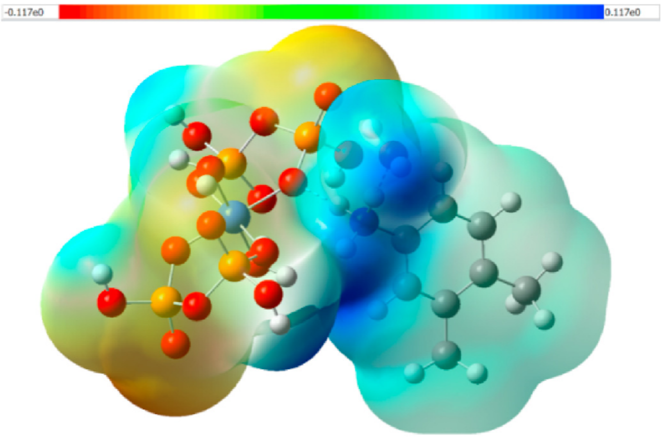

Fig. 8. The molecular electrostatic potential surface of the studied sample calculated at the B3LYP/6-31+G(d,p) level of theory.

3.4. Frontier molecular orbitals analysis

The frontier molecular orbital theory plays an important role in the prediction and explanation of aspects of chemical reactivity and selectivity of chemical reactions. As can be seen from Fig. 7, The HOMO (the highest occupied molecular orbital) is mainly delocalized over 3,4-dimethylanilinium moiety, while the LUMO (the lowest occupied molecular orbital) is mainly delocalized over the Co-L moiety. The band gap gives qualitative information about the charge transfer interaction that occurs within a molecule and is mainly defined as the energy difference between HOMO that acts as electron donor and LUMO that acts as electron acceptor [57,58]. The relatively low gap energy between FMOs (3.45 eV) may indicates the high polarizable, the high reactivity of $(C_8H_{12}N)_2[Co(H_2P_2O_7)_2(H_2O)_2].2H_2O$ as we know from literature [59] and the low molecular stability.

3.5. Molecular electrostatic potential

The Molecular Electrostatic Potential (MEP) map of the title molecule was calculated theoretically at the B3LYP/6-31+G(d,p) level of theory (Fig. 8). The MEP is very valuable in the visualization of the charge distributions, the grasping of the molecular interactions as well as in the

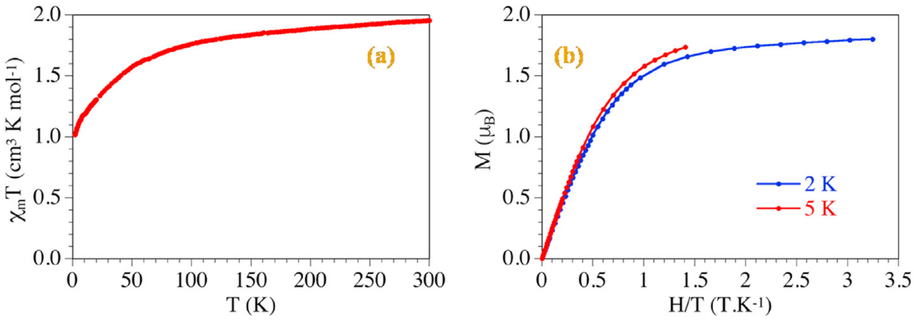

Fig. 9. (a): Temperature dependent magnetic susceptibility for the synthesized compound. **(b).** Isothermal magnetization of $(C_8H_{12}N)_2[Co(H_2P_2O_7)_2(H_2O)_2].2H_2O$.

depicting of the molecular size and shape [60]. The color garden in the plot is in the range between −0.117 a.u. (red) to 0.117 a.u. (blue) for DFT method, the electrostatic potential increases in the order red < orange < yellow < green < blue. The red-colored region is nucleophile, where the density of electrons is higher than the nucleus through the whole of the molecule, the blue color indicates the positive potential and the white region indicates neutral atoms [61,62]. The negative region of the electrostatic potential corresponds to hydrogen bond acceptors while the positive region corresponds to hydrogen bond donors. In accordance with Hirshfeld surface analysis, the blue region around the ammonium group indicates its role as a hydrogen donor, the red regions over oxygen atoms indicates that the lone pairs of oxygen atoms are hydrogen bond acceptors.

3.6. *UV–visible measurement*

The solid state UV–Vis absorption spectrum for $(C_8H_{12}N)_2[Co(H_2P_2O_7)_2(H_2O)_2].2H_2O$, is presented in Fig.S4(a), exhibits three peaks with different intensities and wavelength. The band at 264 nm can be ascribed to the π-π^* transition of the aromatic ring of the organic cation. It corresponding predicted one obtained at B3LYP/6-31+G(d,p) appears at λ_{max} of 273 nm, with a variation of 9 nm with respect to the experimental value (Fig. S4(b)). This absorption band is attributed mainly to the electronic transition HOMO-8→LUMO with oscillator strength of 0.025. The band located at 360 nm probably may originate from the n-π^* transition of the diphosphoric anion. The large band located at 525 nm corresponds to the d-d transition of the cobalt (II) ions which is in good agreement with X-ray analysis. The optical band gap (Eg) can be evaluated using Tauc's method [63] by plotting $(\alpha h\upsilon)^2$ versus hυ (α is the absorption coefficient and hυ is the energy of the incident photon where h represents Planck's constant and υ is the frequency of vibration).

The energy of the incident photon is calculated using the equation:[64]

$$h\upsilon = \frac{1240}{\lambda(nm)}$$

The value of the band gap, offered by the extrapolation of the linear portion of the straight-line portion $(\alpha h\upsilon)^2$ versus hυ, is equal to 2.89 eV. This result proves that the investigated compound is a semiconductor ($0 < Eg = 2.89$ eV < 4 eV) [65,66] and can be useful in multiple applications such as optoelectronics and laser [67].

3.7. *Fluorescence properties*

The photoluminescence spectrum of the title compound excited at ex = 280 nm and studied in the solid state at room temperature is depicted as follows. As displayed in Fig.S5, the luminescence spectrum of the complex is characterized by a broad band centered at 407 nm, which is corresponded probably to the transitions π-π* of the aromatic ring of the organic cation. The emission at 441 nm can be ascribed to the metal–ligand charge transfer.

3.8. *Magnetic properties*

Magnetic susceptibility measurements of the synthesized compound have been performed on powdered sample over the temperature range from 2 to 300 K. Fig. 9(a) depicts the plots of the $\chi_M T$ versus T (where χ_M is the molar magnetic susceptibility per cobalt (II) ion). The $\chi_M T$ value at 300 K is about 1.8 cm^3 K mol^{-1} per formula unit which is well agree with the value observed for an octahedral environment with for $S = \frac{3}{2}$ and the

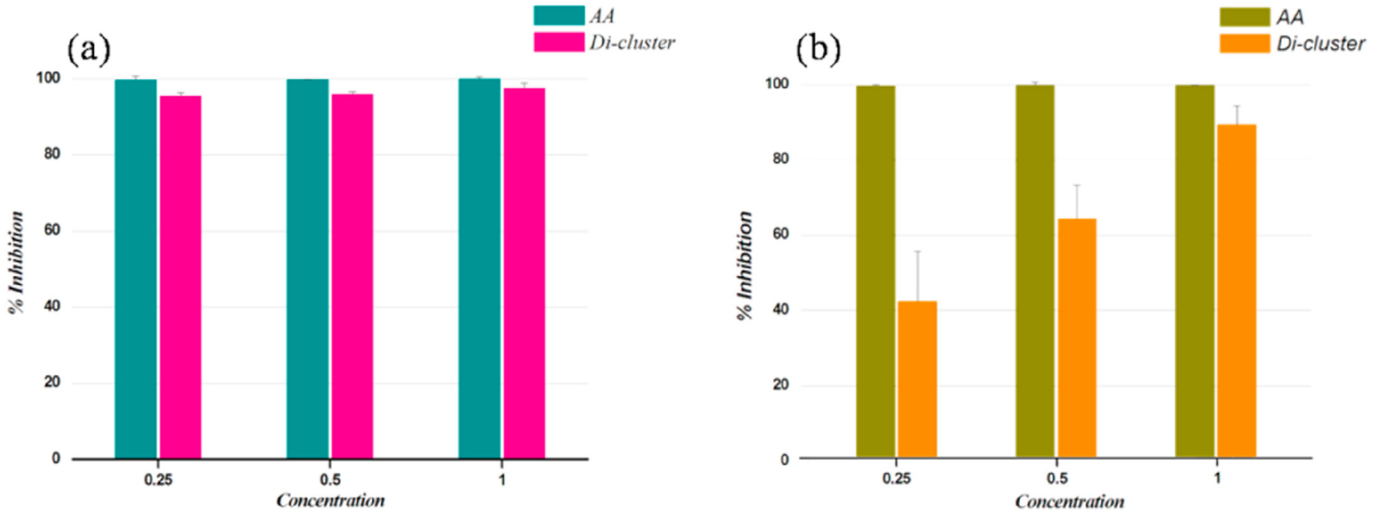

Fig. 10. (a). ABTS radical scavenging activity. **(b).** Ferrous ion chelating activity.

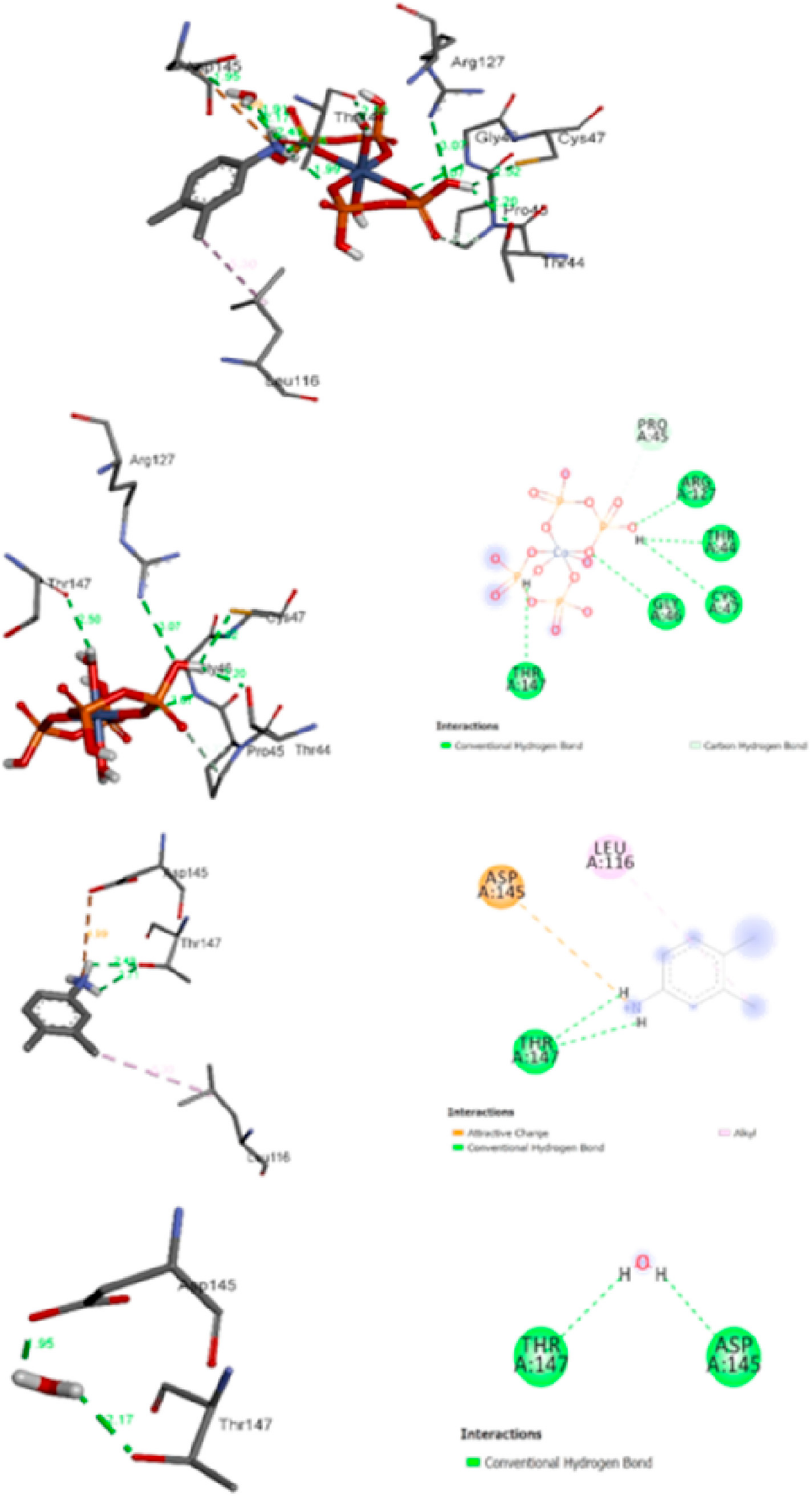

Fig. 11. The interactive plot of docked ligand with the active residues of peroxiredoxin 5.

Lande factor g = 2.1897 with an orbitally degenerate $^4T_1$ single-ion ground state [68,69]. Once the temperature decreases, the value $\chi_M T$ also drops up to the lowest measured temperature 2 K and reaches a minimum value of 1 cm^3 K mol^{-1}. The reason for such behavior is attributed to the effect of spin-orbit coupling rather than the occurrence of an antiferromagnetic exchange interaction between the cobalt (II) centers Co-Co [70].

At 2 K, the magnetization M (H) hysteresis curve increase gradually with increasing of the applied magnetic field H (T) reaching a value of 1.7 μ_B, as can be seen in Fig. 9(b). The isothermal M(H) plots are necessary for a complete analysis of the magnetic properties of the title compound. Hence our sample is antiferromagnetic.

3.9. Antioxidant activities

The antioxidant activity of the synthesized compound was tested in this study against two different radical species, ABTS and FIC at different concentration ranges (0.25, 0.5, 1 mg/mL) and the results were compared with that of ascorbic acid (AA), being used as reference standard. The result of ABTS test was reported in Fig. 10(a). It is observed that the ABTS radical increases with increasing of the complex concentration in the tested range. The percentage of inhibition is 95.4 ± 0.88% for a concentration 0.25 mg/mL and is lower than that of the reference (99.59 ± 1.04% AA) while at 1 mg/mL it is 97.45 ± 1.39% (99.94 ± 0.61% AA).

Fig. 10(b) summarizes the result of the test against Ferrous Ion Chelating (FIC), demonstrated that the title compound has the lowest percentage of inhibition at the high concentration 89.27 ± 5.06% in comparison to the reference compound at the same concentration, the percentage of inhibition is 99.86 ± 0.17%.

3.10. Molecular docking

In an attempt to understand the observed antioxidant activity of the title compound, molecular docking study has been carried out to determine the binding modes between the Co(II)-diphosphate cluster and the active residues of peroxiredoxin 5. The Co(II)-diphosphate cluster-peroxiredoxin 5 complex show negative bending energy of −3.4 $kcalmol^{-1}$, which may indicate the potency of $(C_8H_{12}N)_2[Co(H_2P_2O_7)_2(H_2O)_2].2H_2O$ act as an antioxidant. Fig. 11 displays the binding interaction establishes between the title compound moieties and the active amino acids peroxiredoxin 5 into the binding site. These intermolecular interactions are mainly of hydrogen bonding type. It appears that the Co complex moiety in the Co(II)-diphosphate cluster has the highest contribution to the stability of $(C_8H_{12}N)_2[Co(H_2P_2O_7)_2(H_2O)_2].2H_2O$-peroxiredoxin 5. Indeed, Co complex forms five hydrogen bonding with ARG A127, THRA 44, CYS A47, GLY A46 and THR A147 of distances 3.07, 2.20, 2.52, 3.07 and 2.50 Å, respectively (Fig. 11).

4. Conclusion

A new complex $(C_8H_{12}N)_2[Co(H_2P_2O_7)_2(H_2O)_2].2H_2O$ was synthesized through the method of crystallization. The single crystals are successfully grown from ethanol solution by slow evaporation technique at room temperature. The molecular and crystal structure of the obtained compound has been elucidated by single crystal X-ray diffraction. Our finding belongs to the triclinic system with the $P\bar{1}$ space group. Here, the powder X-ray diffraction confirms the purity of the grown crystal which can induce that the sample is suitable for the measurement of magnetic properties. Besides, the geometrical structure are theoretically calculated by DFT theory and compared with the experimental data, we found that the theoretical values agree fairly well with the experimental one. To further understand the intermolecular interactions in the crystal structure, Hirshfeld surface analysis have been carried out. The major contribution comes from the O⋯H/H⋯O interaction. Very good agreement was observed between the calculated FT-IR spectra and their counterparts from experimental data. Furthermore, Frontier molecular orbital analysis and molecular electrostatic potential map have been calculated by using DFT method with B3LYP/6-31+G(d,p) basis set. Additionally, the optical properties were investigated by absorption and photoluminescence measurements. It is found that the gap energy value of the formed compound is 2.89 eV, in the light of this result, we are able to predict that our finding is a semiconductor. Magnetic measurements were performed and showed that the compound exhibited an antiferromagnetic interaction between the Co(II) centers. To determine the antioxidant activity ABTS free radical scavenging assay and FIC method were used. The results outlined highlight that this class of materials can be considered as a promising candidate as biologically active substance which can be helpful in the field of biological medicine.

Declaration of competing interest

The authors declare that they have no known competing financial interests or personal relationships that could have appeared to influence the work reported in this paper.

Acknowledgements

This work is supported by the Tunisian National Ministry of Higher Education and Scientific Research. A. V. Kindly acknowledges the Academy of Finland (grant no 314343) for financial support.

Supplementary Data

Crystallographic data for the title compound have been deposited at the Cambridge Crystallographic Data Center as supplementary publication (CCDC 2059295). These data can be obtained free of charge at www.ccdc.cam.ac.uk/conts/retrieving.html (or from the Cambridge Crystallographic Data Center, 12, Union Road, Cambridge CB2 1EZ, UK; fax: +44 1223/336 033; mailto: deposit@ccdc.cam.ac.uk).

Appendix A. Supplementary data

Supplementary data to this article can be found online at https://doi.org/10.1016/j.jssc.2021.122319.

References

[1] S.H. Mir, L.A. Nagahara, T. Thundat, P. Mokarian-Tabari, H. Furukawa, A. Khosla, Review-Organic-inorganic hybrid functional materials: an integrated platform for applied technologies, J. Electrochem. Soc. 165 (2018) B3137–B3156, https://doi.org/10.1149/2.0191808jes.

[2] Y. Wang, F. Wang, D. Wang, A. Li, G. Chen, H. Xiong, Y. Wei, P. Wu, Z. Xiao, Synthesis and structure studies of a new hexavanadate-glycine hybrid with high antitumor activities, J. Mol. Struct. 1201 (2020) 127138, https://doi.org/10.1016/j.molstruc.2019.127138.

[3] M. Gemili, Y. Nural, E. Keleş, B. Aydıner, N. Seferoğlu, M. Ülger, E. Şahin, S. Erat, Z. Seferoğlu, Novel highly functionalized 1,4-naphthoquinone 2-iminothiazole hybrids: synthesis, photophysical properties, crystal structure, DFT studies, and anti(myco)bacterial/antifungal activity, J. Mol. Struct. 1196 (2019) 536–546, https://doi.org/10.1016/j.molstruc.2019.06.087.

[4] I.B. Hadj Sadok, F. Hajlaoui, H.B. Ayed, N. Ennaceur, M. Nasri, N. Audebrand, T. Bataille, N. Zouari, Crystal packing, high-temperature phase transition, second-order nonlinear optical and biological activities in a hybrid material: $[(S)\text{-}C_7H_{16}N_2][CuBr_4]$, J. Mol. Struct. 1167 (2018) 316–326, https://doi.org/10.1016/j.molstruc.2018.05.011.

[5] M.S. Lassoued, M.S.M. Abdelbaky, R.M. Meroño, A. Gadri, S. Ammar, A. Ben Salah, S. García-Granda, Structure, spectroscopic measurement, thermal studies and optical properties of a new hybrid compound of aquapentachloroindoidate(III) complex, J. Mol. Struct. 1142 (2017) 73–79, https://doi.org/10.1016/j.molstruc.2017.04.037.

[6] R. Henchiri, N. Ennaceur, M. Cordier, I. Ledoux-Rak, E. Elaloui, Synthesis, X-ray crystal structure and highly non-linear optical properties of inorganic-organic hybrid compound: 1,4-Diazbicyclo-octane oxonium tri- nitrates single crystal, J. Phys. Chem. Solid. 106 (2017) 58–64, https://doi.org/10.1016/j.jpcs.2017.02.011.

[7] K. Boopathi, S.M. Babu, R. Jagan, P. Ramasamy, Synthesis, crystal structure and growth of a new inorganic- organic hybrid compound for nonlinear optical

applications: aquadiiodo (3-aminopropanoic acid) cadmium (II), J. Phys. Chem. Solid. 111 (2017) 419–430, https://doi.org/10.1016/j.jpcs.2017.08.038.

[8] X.-W. Cai, Y.-Y. Zhao, H. Li, C.-P. Huang, Z. Zhou, Lead-free/rare earth-free Green-light-emitting crystal based on organic-inorganic hybrid $[(C_{10}H_{16}N)_2][MnBr_4]$ with high emissive quantum yields and large crystal size, J. Mol. Struct. 1161 (2018) 262–266, https://doi.org/10.1016/j.molstruc.2018.01.093.

[9] Q. Deng, H. Xiao, Q. Fang, Q. Cai, Y. Han, T. Cai, A solid-state supramolecular hybrid complex based on dimethylammonium ions and silicon molybdate: crystal structure, photochromic properties and catalytic performance, J. Solid State Chem. 271 (2019) 81–87, https://doi.org/10.1016/j.jssc.2018.12.046.

[10] L.H. Abdel-Rahman, A.M. Abu-Dief, E.F. Newair, S.K. Hamdan, Some new nano-sized Cr(III), Fe(II), Co(II), and Ni(II) complexes incorporating 2-((E)-(pyridine-2-ylimino)methyl)napthalen-1-ol ligand: structural characterization, electrochemical, antioxidant, antimicrobial, antiviral assessment and DNA interaction, J. Photochem. Photobiol. B Biol. 160 (2016) 18–31, https://doi.org/10.1016/j.jphotobiol.2016.03.040.

[11] N.H. Gokhale, S.B. Padhye, S.L. Croft, H.D. Kendrick, W. Davies, C.E. Anson, A.K. Powell, Transition metal complexes of buparvaquone as potent new antimalarial agents. 1. Synthesis, X-ray crystal-structures, electrochemistry and antimalarial activity against Plasmodium falciparum, J. Inorg. Biochem. 95 (2003) 249–258, https://doi.org/10.1016/s0162-0134(03)00134-x.

[12] V. Kamat, D. Kokare, K. Naik, A. Kotian, S. Naveen, S.R. Dixit, N.K. Lokanath, S.D. Joshi, V.K. Revankar, Transition metal complexes of 2-(2-(1H-benzo[d]imidazole-2-yl)hydrazono)propan-1-ol: synthesis, characterization, crystal structures and anti-tuberculosis assay with docking studies, Polyhedron 127 (2017) 225–237, https://doi.org/10.1016/j.poly.2017.02.010.

[13] J.A.D. Batista, L. Oliveira, T.A. Moura, V.C. dos Anjos, M.J.V. Bell, M.S. Rocha, On the use of Europium (Eu) for designing new metal-based anticancer drugs, Biochem. Biophys. Res. Commun. 531 (2020) 372–376, https://doi.org/10.1016/j.bbrc.2020.07.080.

[14] W. Liu, Y. Zhong, X. Wang, C. Zhuang, J. Chen, D. Liu, W. Xiao, Y. Pan, J. Huang, J. Liu, A porous Cu(II)-based metal-organic framework carrier for pH-controlled anticancer drug delivery, Inorg. Chem. Commun. 111 (2020) 107675, https://doi.org/10.1016/j.inoche.2019.107675.

[15] G.L. Silva, J.S.M. Dias, H.V.R. Silva, J.D.S. Teixeira, I.R.B. De Souza, E.T. Guimarães, D.R. de Magalhães Moreira, M.B.P. Soares, M.I.F. Barbosa, A.C. Doriguetto, Synthesis, crystal structure and leishmanicidal activity of new trimethoprim Ru(III), Cu(II) and Pt(II) metal complexes, J. Inorg. Biochem. 205 (2020) 111002, https://doi.org/10.1016/j.jinorgbio.2020.111002.

[16] J.M. Méndez-Arriaga, A. Rodríguez-Diéguez, M. Sánchez-Moreno, In vitro leishmanicidal activity of copper (II) 5,7-dimethyl-1,2,4-triazolo[1,5-a]pyrimidine complex and analogous transition metal series, Polyhedron 176 (2020) 114272, https://doi.org/10.1016/j.poly.2019.114272.

[17] M. Arsenijevic, M. Milovanovic, S. Jovanovic, N. Arsenijevic, B.S. Markovic, M. Gazdic, V. Volarevic, In vitro and in vivo anti-tumor effects of selected platinum(IV) and dinuclear platinum(II) complexes against lung cancer cells, J. Biol. Inorg. Chem. 22 (2017) 807–817, https://doi.org/10.1007/s00775-017-1459-y.

[18] K.G. Samper, S.C. Marker, P. Bayón, S.N. MacMillan, I. Keresztes, Ò. Palacios, J.J. Wilson, Anticancer activity of hydroxy- and sulfonamide-azobenzene platinum(II) complexes in cisplatin-resistant ovarian cancer cells, J. Inorg. Biochem. 174 (2017) 102–110, https://doi.org/10.1016/j.jinorgbio.2017.06.003.

[19] A. Eskandari, A. Kundu, S. Ghosh, K. Suntharalingam, A triangular platinum(II) multinuclear complex with cytotoxicity towards breast cancer stem cells, Angew. Chem. Int. Ed. 58 (2019) 12059–12064, https://doi.org/10.1002/anie.201905389.

[20] S. Dasari, P.B. Tchounwou, Cisplatin in cancer therapy: molecular mechanisms of action, Eur. J. Pharmacol. 740 (2014) 364–378, https://doi.org/10.1016/j.ejphar.2014.07.025.

[21] M. Heidari Khoee, S. Khoee, M. Lotfi, Synthesis of titanium dioxide nanotubes with liposomal covers for carrying and extended release of 5-FU as anticancer drug in the treatment of HeLa cells, Anal. Biochem. 572 (2019) 16–24, https://doi.org/10.1016/j.ab.2019.02.027.

[22] L. Messori, G. Marcon, Gold complexes in the treatment of rheumatoid arthritis, Met. Ion. Biol. Syst. 41 (2004) 279–304, https://doi.org/10.1201/9780203913703.ch9.

[23] A.K. Srivastava, M.Z. Mehdi, Insulino-mimetic and anti-diabetic effects of vanadium compounds, Diabet. Med. 22 (2005) 2–13, https://doi.org/10.1111/j.1464-5491.2004.01381.x.

[24] N. Şahin, İ. Yıldırım, N. Özdemir, N. Gürbüz, İ. Özdemir, First used of Alkylbenzimidazole-Cobalt(II) complexes as a catalyst for the N-Alkylation of amines with alcohols under solvent-free medium, J. Organomet. Chem. 918 (2020) 121285, https://doi.org/10.1016/j.jorganchem.2020.121285.

[25] A. Marir, T.N. Mouas, B. Anak, E. Jeanneau, A. Djedouani, L. Aribi-Zouioueche, F. Rabilloud, Cobalt(II), Nickel(II) and Zinc(II) complexes based on DHA: synthesis, X-ray crystal structure, antibacterial activity and DFT computational studies, J. Mol. Struct. 1217 (2020) 128353, https://doi.org/10.1016/j.molstruc.2020.128353.

[26] F.J. Teixeira, L.S. Flores, L.B.L. Escobar, T.C. dos Santos, M.I. Yoshida, M.S. Reis, S. Hill, C.M. Ronconi, C.C. Corrêa, A 3D interpenetrated Co(II)-glutarate coordination polymer: synthesis, crystal structure, magnetic and adsorption properties, Inorg. Chim. Acta. 511 (2020) 119791, https://doi.org/10.1016/j.ica.2020.119791.

[27] J.M. Frost, K.L.M. Harriman, M. Murugesu, The rise of 3-d single-ion magnets in molecular magnetism: towards materials from molecules? Chem. Sci. 7 (2016) 2470–2491, https://doi.org/10.1039/C5SC03224E.

[28] A.K. Bar, C. Pichon, J.-P. Sutter, Magnetic anisotropy in two- to eight-coordinated transition–metal complexes: recent developments in molecular magnetism, Coord. Chem. Rev. 308 (2016) 346–380, https://doi.org/10.1016/j.ccr.2015.06.013.

[29] S. Kumar, A. Nanda, Pharmaceutical cocrystals: an overview, Indian J. Pharmaceut. Sci. 79 (2017) 858–871, https://doi.org/10.4172/pharmaceutical-sciences.1000302.

[30] B. Poljsak, D. Šuput, I. Milisav, Achieving the balance between ROS and antioxidants: when to use the synthetic antioxidants, Oxid. Med. Cell. Longev. 2013 (2013) 956792, https://doi.org/10.1155/2013/956792.

[31] I. Liguori, G. Russo, F. Curcio, G. Bulli, L. Aran, D. Della-Morte, G. Gargiulo, G. Testa, F. Cacciatore, D. Bonaduce, P. Abete, Oxidative stress, aging, and diseases, Clin. Interv. Aging 13 (2018) 757–772, https://doi.org/10.2147/CIA.S158513.

[32] R. D'Oria, R. Schipani, A. Leonardini, A. Natalicchio, S. Perrini, A. Cignarelli, L. Laviola, F. Giorgino, The role of oxidative stress in cardiac disease: from physiological response to injury factor, Oxid. Med. Cell. Longev. 2020 (2020) 5732956, https://doi.org/10.1155/2020/5732956.

[33] N. Amiri, S. Nouir, M. Hajji, T. Roisnel, T. Guerfel, G. Simonneaux, H. Nasri, Synthesis, structure, photophysical properties and biological activity of a cobalt(II) coordination complex with 4,4′-bipyridine and porphyrin chelating ligands, J. Saudi Chem. Soc 23 (2019) 781–794, https://doi.org/10.1016/j.jscs.2019.03.003.

[34] K. Chkirate, S. Fettach, K. Karrouchi, N.K. Sebbar, E.M. Essassi, J.T. Mague, S. Radi, M. El Abbes Faouzi, N.N. Adarsh, Y. Garcia, Novel Co(II) and Cu(II) coordination complexes constructed from pyrazole-acetamide: effect of hydrogen bonding on the self assembly process and antioxidant activity, J. Inorg. Biochem. 191 (2019) 21–28, https://doi.org/10.1016/j.jinorgbio.2018.11.006.

[35] G. Sheldrick, Shelxt - integrated space-group and crystal-structure determination, Acta Crystallogr. A 71 (2015) 3–8, https://doi.org/10.1107/S2053273314026370.

[36] G.M. Sheldrick, Crystal structure refinement with SHELXL, Acta Crystallogr. C 71 (2015) 3–8, https://doi.org/10.1107/S2053229614024218.

[37] K. Brandenburg, DIAMOND Version 2, 1998, .0.

[38] S. Wolff, D. Grimwood, J. McKinnon, M. Turner, D. Jayatilaka, M. Spackman, Crystal Explorer, The University of Western Australia Perth, Australia, 2012.

[39] M.J. Frisch, G.W. Trucks, H.B. Schlegel, G.E. Scuseria, M.A. Robb, J.R. Cheeseman, G. Scalmani, V. Barone, G.A. Petersson, H. Nakatsuji, X. Li, M. Caricato, A.V. Marenich, J. Bloino, B.G. Janesko, R. Gomperts, B. Mennucci, H.P. Hratchian, J.V. Ortiz, A.F. Izmaylov, J.L. Sonnenberg, D. Williams-Young, F. Ding, F. Lipparini, F. Egidi, J. Goings, B. Peng, A. Petrone, T. Henderson, D. Ranasinghe, V.G. Zakrzewski, J. Gao, N. Rega, G. Zheng, W. Liang, M. Hada, M. Ehara, K. Toyota, R. Fukuda, J. Hasegawa, M. Ishida, T. Nakajima, Y. Honda, O. Kitao, H. Nakai, T. Vreven, K. Throssell, J.A. Montgomery, Jr, J.E. Peralta, F. Ogliaro, M.J. Bearpark, J.J. Heyd, E.N. Brothers, K.N. Kudin, V.N. Staroverov, T.A. Keith, R. Kobayashi, J. Normand, K. Raghavachari, A.P. Rendell, J.C. Burant, S.S. Iyengar, J. Tomasi, M. Cossi, J.M. Millam, M. Klene, C. Adamo, R. Cammi, J.W. Ochterski, R.L. Martin, K. Morokuma, O. Farkas, J.B. Foresman, D.J. Fox, Gaussian, Inc., Wallingford CT, 2016..

[40] J. Tomasi, B. Mennucci, R. Cammi, Quantum mechanical continuum solvation models, Chem. Rev. 105 (2005) 2999–3094, https://doi.org/10.1021/cr9904009.

[41] C.I.G. Tuberoso, M. Boban, E. Bifulco, D. Budimir, F.M. Pirisi, Antioxidant capacity and vasodilatory properties of Mediterranean food: the case of Cannonau wine, myrtle berries liqueur and strawberry-tree honey, Food Chem. 140 (2013) 686–691, https://doi.org/10.1016/j.foodchem.2012.09.071.

[42] N. Singh, P.S. Rajini, Free radical scavenging activity of an aqueous extract of potato peel, Food Chem. 85 (2004) 611–616, https://doi.org/10.1016/j.foodchem.2003.07.003.

[43] G.M. Morris, R. Huey, W. Lindstrom, M.F. Sanner, R.K. Belew, D.S. Goodsell, A.J. Olson, AutoDock4 and AutoDockTools4: automated docking with selective receptor flexibility, J. Comput. Chem. 30 (2009) 2785–2791, https://doi.org/10.1002/jcc.21256.

[44] J.P. Declercq, C. Evrard, A. Clippe, D.V. Stricht, A. Bernard, B. Knoops, Crystal structure of human peroxiredoxin 5, a novel type of mammalian peroxiredoxin at 1.5 A resolution, J. Mol. Biol. 311 (2001) 751–759, https://doi.org/10.1006/jmbi.2001.4853.

[45] I.M.M. Othman, M.A.M. Gad-Elkareem, E.H. Anouar, M. Snoussi, K. Aouadi, A. Kadri, Novel fused pyridine derivatives containing pyrimidine moiety as prospective tyrosyl-tRNA synthetase inhibitors: design, synthesis, pharmacokinetics and molecular docking studies, J. Mol. Struct. 1219 (2020) 128651, https://doi.org/10.1016/j.molstruc.2020.128651.

[46] S. Cherni, F. Zid, A. Driss, Crystal structure of a [(dihydrogen pyrophosphato-K^2O,O′) bis (1,10-phenanthroline-N,N′) nickel(II)] 2.5-hydrate $[Ni(H_2P_2O_7)(C_{12}H_8N_2)_2]\cdot 2.5H_2O$, J. Struct. Chem. 57 (2016) 1671–1674, https://doi.org/10.1134/S0022476616080254.

[47] A. Elboulali, S. Akriche, M. Rzaigui, Bis(2-meth–oxy-benzyl-ammonium) di-aqua-bis-(di-hydrogen diphosphato-κ2O,O′)cobaltate(II) dihydrate, Acta Crystallogr. 70 (2014) m145–m146, https://doi.org/10.1107/S1600536814006102.

[48] J.J. McKinnon, M.A. Spackman, A.S. Mitchell, Novel tools for visualizing and exploring intermol-ecular interactions in molecular crystals, Acta Crystallogr. B 60 (2004) 627–668, https://doi.org/10.1107/S0108768104020300.

[49] M.A. Spackman, P.G. Byrom, A novel definition of a molecule in a crystal, Chem. Phys. Lett. 267 (1997) 215–220, https://doi.org/10.1016/S0009-2614(97)00100-0.

[50] L. Guelmami, A. Gharbi, A. Jouini, Synthesis and characterization of a new 2,4,6-triaminopyridinium dihydrogendiphosphate dihydrate $(C_4H_8N_5)_2H_2P_2O_7\cdot 2H_2O$, Mater. Res. Bull. 44 (2009) 549–554, https://doi.org/10.1016/j.materresbull.2008.07.013.

[51] A. Elboulali, S. Akriche, M. Rzaigui, S.S. Al-Deyab, Structural and electrical conductivity properties of a newly synthesized 3-methoxybenzylammonium cation diphosphate, E-J. Chem. 9 (2012) 2029–2036, https://doi.org/10.1155/2012/731585.

[52] N. Jouini, L. BenHamada, A. Jouini, Crystal structure of a new organic condensed phosphate $(C_6H_9N_3O)H_2P_2O_7$, Mater. Res. Bull. 42 (2007) 56–63, https://doi.org/10.1016/j.materresbull.2006.05.018.

[53] M. Stomp, J. Huisman, L.J. Stal, H.C. Matthijs, Colorful niches of phototrophic microorganisms shaped by vibrations of the water molecule, ISME J. 1 (2007) 271–282, https://doi.org/10.1038/ismej.2007.59.

[54] S. Guidara, H. Feki, Y. Abid, Molecular structure, NLO, MEP, NBO analysis and spectroscopic characterization of 2,5-dimethylanilinium dihydrogen phosphate with experimental (FT-IR and FT-Raman) techniques and DFT calculations, Spectrochim. Acta, Part A 133 (2014) 856–866, https://doi.org/10.1016/j.saa.2014.06.021.

[55] V. Sangeetha, M. Govindarajan, N. Kanagathara, M.K. Marchewka, S. Gunasekaran, G. Anbalagan, Vibrational, DFT, thermal and dielectric studies on 3-nitrophenol-1,3,5-triazine-2,4,6-triamine (2/1), Spectrochim. Acta, Part A 118 (2014) 1025–1037, https://doi.org/10.1016/j.saa.2013.09.097.

[56] E. Temel, C. Alaşalvar, H. Gökçe, A. Güder, Ç. Albayrak, Y.B. Alpaslan, G. Alpaslan, N. Dilek, DFT calculations, spectroscopy and antioxidant activity studies on (E)-2-nitro-4-[(phenylimino)methyl]phenol, Spectrochim. Acta, Part A 136 (2015) 534–546, https://doi.org/10.1016/j.saa.2014.09.067.

[57] V. Choudhary, A. Bhatt, D. Dash, N. Sharma, DFT calculations on molecular structures, HOMO-LUMO study, reactivity descriptors and spectral analyses of newly synthesized diorganotin(IV) 2-chloridophenylacetohydroxamate complexes, J. Comput. Chem. 40 (2019) 2354–2363, https://doi.org/10.1002/jcc.26012.

[58] A. Sakka, A. Jellali, B. Hamdi, M.S.M. Abdelbaky, H. Naïli, S. García-Granda, R. Zouari, Structure, spectroscopic measurement, thermal studies and optical properties of a new non-centrosymmetric hybrid compound, J. Mol. Struct. 1198 (2019) 126867, https://doi.org/10.1016/j.molstruc.2019.07.114.

[59] P. Sivajeyanthi, M. Jeevaraj, S.J. Kavitha, M. Hemamalini, K. Balasubramani, Synthesis, crystal structure, Hirshfeld surface analysis and HOMO–LUMO energy levels of *(E)-N′*-(naphthalen-1-ylmethylene)-4-nitrobenzohydrazide, Chem. Data. Collect. 20 (2019) 100194, https://doi.org/10.1016/j.cdc.2019.100194.

[60] Z.S. Şahin, H. Şenöz, H. Tezcan, O. Büyükgüngör, Synthesis, spectral analysis, structural elucidation and quantum chemical studies of (E)-methyl-4-[(2-phenylhydrazono) methyl] benzoate, Spectrochim. Acta, Part A 143 (2015) 91–100, https://doi.org/10.1016/j.saa.2015.02.032.

[61] R. Rahmani, N. Boukabcha, A. Chouaih, F. Hamzaoui, S. Goumri-Said, On the molecular structure, vibrational spectra, HOMO-LUMO, molecular electrostatic potential, UV–Vis, first order hyperpolarizability, and thermodynamic investigations of 3-(4-chlorophenyl)-1-(1yridine-3-yl) prop-2-en-1-one by quantum chemistry calculations, J. Mol. Struct. 1155 (2018) 484–495, https://doi.org/10.1016/j.molstruc.2017.11.033.

[62] A.M. Bayoumy, M. Ibrahim, A. Omar, Mapping molecular electrostatic potential (MESP) for fulleropyrrolidine and its derivatives, Opt. Quant. Electron. 52 (2020) 346–359, https://doi.org/10.1007/s11082-020-02467-6.

[63] J. Tauc, Optical properties and electronic structure of amorphous Ge and Si, Mater. Res. Bull. 3 (1968) 37–46, https://doi.org/10.1016/0025-5408(68)90023-8.

[64] B. Uma, K. Sakthi Murugesan, S. Krishnan, R. Jayavel, B. Milton Boaz, Growth, optical, thermal and dielectric studies of a highly polarisable semi organic NLO crystal: bis d-phenyl glycinium sulphate monohydrate, Mater. Chem. Phys. 142 (2013) 659–666, https://doi.org/10.1016/j.matchemphys.2013.08.018.

[65] K. Karoui, A new hybrid layered perovskite $[CH_3–C_6H_4–NH_3]_2ZnBr_4$: synthesis, crystal structure, optical and electrical properties, J. Mol. Struct. 1203 (2020) 127430, https://doi.org/10.1016/j.molstruc.2019.127430.

[66] O. Ben Moussa, H. Chebbi, M.F. Zid, Synthesis, crystal structure, vibrational study, optical properties and Hirshfeld surface analysis of bis(2,6-diaminopyridinium) tetrachloridocobaltate(II) monohydrate, J. Mol. Struct. 1180 (2019) 72–80, https://doi.org/10.1016/j.molstruc.2018.11.077.

[67] H.-J. Li, Y.-L. Liu, X.-G. Chen, J.-X. Gao, Z.-X. Wang, W.-Q. Liao, High-temperature dielectric switching and photoluminescence in a corrugated lead bromide layer hybrid perovskite semiconductor, Inorg. Chem. 58 (2019) 10357–10363, https://doi.org/10.1021/acs.inorgchem.9b01538.

[68] B.-L. Li, X.-Y. Wang, X. Zhu, S. Gao, Y. Zhang, Synthesis, crystal structure and magnetic behavior of two cobalt coordination polymers with 1,2-bis(1,2,4-triazol-1-yl)ethane and dicyanamide, Polyhedron 26 (2007) 5219–5224, https://doi.org/10.1016/j.poly.2007.07.044.

[69] Y.-L. Xu, J. Zhang, L.-S. Chen, Y.-Y. Zeng, J.-R. Zhou, C.-L. Ni, W.-X. Zheng, Crystal structure, spectroscopic, non-linear optical, magnetic properties and DFT studies of bis(2-aminopyridinium) tetrachlorocobaltate(II), J. Mol. Struct. 1222 (2020) 128902, https://doi.org/10.1016/j.molstruc.2020.128902.

[70] A. Laachir, F. Rhoufal, S. Guesmi, E.M. Ketatni, L. Jouffret, E.K. Hlil, N. Sergent, S. Obbade, F. Bentiss, Cobalt(II) coordination complex with 2,5-bis(pyridine-2-yl)-1,3,4-thiadiazole and thiocyanate as co-ligand: synthesis, crystal structure, Hirshfeld surface analysis, spectroscopic, thermal and magnetic properties, J. Mol. Struct. 1208 (2020) 127892, https://doi.org/10.1016/j.molstruc.2020.127892.